Revision 3

How Clay Delamination Supports Aseismic Slip

Huijun Zhou[1,2,3], Meng Chen[1,2,*], Runliang Zhu[1,2,3], Jianxi Zhu[1,2,3], and Hongping He[1,2,3]

[1] CAS Key Laboratory of Mineralogy and Metallogeny/Guangdong Provincial Key Laboratory of Mineral Physics and Materials, Guangzhou Institute of Geochemistry, Institutions of Earth Science, Chinese Academy of Sciences (CAS), Guangzhou 510640, China.

[2] CAS Center for Excellence in Deep Earth Science, Guangzhou 510640, China.

[3] University of Chinese Academy of Sciences, Beijing 100049, China.

Corresponding author: Meng Chen

Tel: 86-020-85290252

Fax: 86-020-85290252

E-mail address: chenmeng@gig.ac.cn (Meng Chen)

Abstract

Aseismic slip is stable fault slip, which allows strain relieved smoothly. Aseismic slip prevents the earthquake propagation but it could nucleate an earthquake elsewhere. Understanding the mechanism of aseismic slip is promising in revealing the seismic cycle. Experimental evidences showed clay-rich fault gouge bears a low friction strength and the friction is strengthened with slip velocity (velocity-strengthening), which were thought to support aseismic slip. Clay minerals are constituted of platy crystalline layers with water intercalated between them, which may act as a lubricant. Sliding between clay layers was suspected to support aseismic slip, but lacking a clarified mechanistic insight. We use non-equilibrium molecular dynamics simulations to show that shear-induced interlayer sliding is frictionally weak and velocity-strengthening, which evidences the role of clay minerals in aseismic slip. We find that interlayer water is a viscous fluid at most times, which explains the shear response of interlayer sliding. Depending on temperature and pressure conditions, intercalated water can be monolayer or bilayer, fluidic or ice-like. Shear induces ice-like water transform into fluidic water, which happens as a stick-slip phenomenon reflecting a first-order transition. Increased pore fluid pressure leads to the transformation from monolayer to bilayer intercalated water, resulting in a lower friction strength and enhanced velocity-strengthening behavior. Our work suggests that disclosing the hydration state of a clay mineral is preliminary when studying the fault mechanics.

INTRODUCTION

Earthquakes arise as a consequence of frictional instabilities that cause stress accumulated over years to be relieved in sudden stick-slip events along the fault. Slip occurs rapidly as a rupture dynamically propagates over the fault surface, which generates seismic waves (Carlson et al. 1994; Scholz 1998). In contrast, stable creeping fault allows strain relieved smoothly and aseismically. Geodetic and seismological observations and geological records have shown a transition between aseismic slip and seismic rupture within the same fault zone (Avouac 2015; Bürgmann et al. 2000; Kawamura et al. 2012; Liu et al. 2020; Maurer and Johnson 2014; McGuire et al. 2012; Perfettini and Avouac 2014; Tarling et al. 2018). Aseismic slip or stable creep prevents the earthquake propagation along the fault, but the strain accumulation due to aseismic slip could nucleate an earthquake beyond the creeping fault zone. As aseismic slip is a common phenomenon in the earthquake preparatory phase, uncovering the underlying physics of this process is promising in Earthquake forecast (Collettini et al. 2019; Kawamura et al. 2012).

Whether a slip is stable or unstable depends on the velocity dependence of the steady-state friction. Sliding begins when shear stress reaches the Coulomb-Mohr failure criterion (Handin 1969). Once sliding, the Amontons' law characterizes the relationship between shear (τ) and effective normal stress ($P_\sigma - P_f$, in which P_σ is the normal stress and P_f is the pore fluid pressure):

$$\tau = \mu_d\left(P_\sigma - P_f\right) \tag{1}$$

where μ_d is the dynamic friction coefficient (Collettini et al. 2019). Materials which

exhibit velocity-strengthening behavior, that is, μ_d in the steady-state sliding regime increases with velocity, only produce stable creep; while velocity-weakening materials may exhibit either unstable stick-slip or conditionally stable behavior (Marone 1998; Scholz 1998). Based on the Dieterich–Ruina constitutive law, or the rate and state friction (RSF) law (Baumberger and Caroli 2006; Kawamura et al. 2012; Scholz 1998), the steady-state friction coefficient scales with the logarithm of sliding velocity v:

$$\mu_d = \mu_0 + (a - b) \ln\left(\frac{v}{v_0}\right) \tag{2}$$

If $a - b \geq 0$, the material is velocity-strengthening, otherwise it is velocity-weakening. Although the RSF law generally applies to rock, papers, wood, metals, and plastics (Heslot et al. 1994; Marone 1998), limitations of it have been reported, e.g., it no longer holds at high sliding velocity (Im et al. 2020; Kawamura et al. 2012). The microphysical foundation of the RSF law is that, creep at asperity junctions between grains follows an Arrhenius activated rate process (Putelat et al. 2011; Rice et al. 2001). However, this foundation might be lost when grains are more separated by melt or fluid (Di Toro et al. 2004; Hirose and Shimamoto 2005; Mizoguchi et al. 2006) and asperity junctions become rare. In such cases, the materials of fault gouge can be seen as amorphous soft solid. The shearing flow of amorphous solid in the steady state manifests a power law dependence of shear stress with shear rate (Liu et al. 2021; Nicolas et al. 2018; Tsai et al. 2021), which is a regime distinct from that follows the RSF law.

The material compositions of fault gouge primarily determine the slip stability.

Gouges rich in phyllosilicate or clay minerals, which present crystallographic preferred orientation fabric (Fig. 1), were speculated to support stable creep (Avouac 2015; Carpenter et al. 2012; Collettini et al. 2019; French et al. 2015; Holdsworth 2004; Lockner et al. 2011). Clay minerals are constituted of platy crystalline layers which weakly interacts with each other through electrostatic, van der Waals, or hydration forces (Smith et al. 2006; Whitley and Smith 2004). Local slip between water-lubricated smectite (a typical clay mineral) layers was suggested during shear (Aretusini et al. 2019). We speculate that some clay layers constitute "hot spots" (Amon et al. 2012; Pons et al. 2016). Local plastic events in hot spots, i.e., slips between layers, support the macroscopic plastic deformation, i.e., fault creep. However, the quantitative connection between fault stability and microscopic interlayer slips is still lacking. The RSF law is a macroscopic view of the shear deformation and it is phenomenological. It would be interesting to see whether the microscopic interlayer slip follows a similar form as the RSF law.

Figure 1

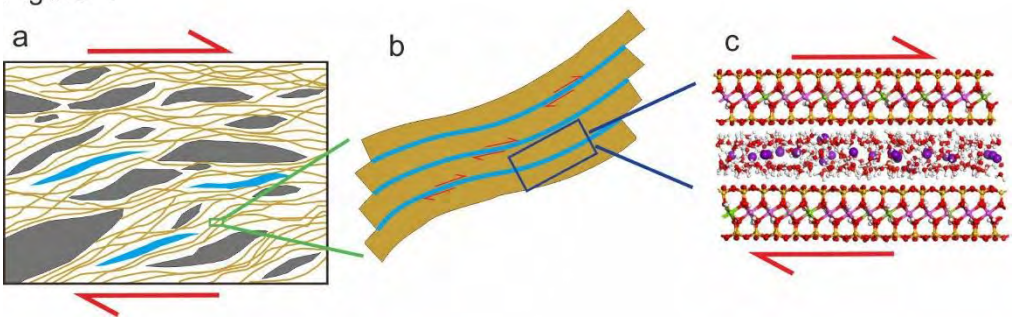

FIGURE 1. Schematic of the relationship between plastic deformation of fault gouge and local slip between clay layers. (a) Fault gouge with large solid grains (grey particles), phyllosilicate or clay minerals (brown lines), and pore water (blue zone). (b) Local slip between clay layers. (c)

Atomic model of a clay mineral. Si, Al, Mg, Na, O, H atoms are in yellow, pink, green, purple, red, and white, respectively.

Slip frictions of lubricants (e.g., water film) confined between surfaces were widely investigated with shear experiments and non-equilibrium molecular dynamics (NEMD) simulations (de Wijn and Pettersson 2017; Dhopatkar et al. 2016; Diao and Espinosa-Marzal 2018; Ma et al. 2015; Xu and Leng 2018; Xu et al. 2020). With water as lubricant, the interfacial structure and phase state or organization of water molecules have specific effects on friction between surfaces (Chen et al. 2015; de Wijn and Pettersson 2017; Dhopatkar et al. 2016; Jinesh and Frenken 2006; Ma et al. 2015; Ortiz-Young et al. 2013; Vilhena et al. 2016). We design NEMD simulations for the following goals: (1) to verify the possibility whether clay layers act as hot spots which support the shear deformation of fault gouge; (2) to disclose whether the interlayer sliding is velocity-strengthening and explain why a clay mineral promotes aseismic slip; (3) to relate the shear behavior with the phase state of the clay interlayer water.

Temperature, normal stress, and pore fluid pressure are environmental variables which affect slip stability (Avouac 2015; French et al. 2015; Yang and Juanes 2018). These variables have influences on the interlayer hydration state of smectite (Smith et al. 2006; Whitley and Smith 2004; Zhou et al. 2020), which in turn affects lubrication between layers. Thus, first of all, the interlayer hydration state under different environmental conditions is determined in this study, through combining equilibrium

molecular dynamics (EMD) simulations and thermodynamic integrations (TI). Hence, through deriving the mechanical property of a hydration state under the same condition with NEMD simulations, the influences of those variables are clarified.

METHODS

Equilibrium molecular dynamics simulations

Arizona-type montmorillonite (unit-cell formula: $(M^{x+})_{1/x}[Al_3Mg][Si_8]O_{20}(OH)_4 \bullet nH_2O$) was chosen as the smectite (clay mineral) model here, which bears only octahedral charges (Hensen et al. 2001; Tambach et al. 2004) and the intercalated cation M^{x+} is Na^+ in this study (Fig. 2). The basic TOT layer (a layer consists of two tetrahedral and one octahedral sheets) of the model was based on the structure of pyrophyllite (Lee and Guggenheim 1981). We built a 7 × 4 × 4 supercell of pyrophyllite. In each unit cell, there is a Mg atom replaced by an Al atom according to the formula of Arizona-type montmorillonite. Any two substitution sites are not adjacent. The range of water content (n) in this study is 0–18.92. The upper bound of the studied water content was determined so as to cover monolayer, bilayer, and trilayer hydration states (Zhou et al. 2020). Water molecules were inserted into the enlarged interlayer according to n. A total of 29 systems with different n were built. Three-dimensional periodic boundary conditions were applied. The electrostatic interaction was evaluated using the particle-mesh Ewald method (Darden et al. 1993; Essmann et al. 1995). The cut-off radius for the short-range non-bonded interactions was set to 1.2 nm. The ClayFF force field (Cygan et al. 2004) was used to describe

atoms in layers of smectite. Water molecules were described by the SPC/E model (Berendsen et al. 1987). The force field parameters of Na^+ were adopted by that proposed by Smith and Dang (1994). Those parameters have long been used in conjunction with the ClayFF forcefield and verified to well deliver properties of Na^+-intercalated smectite (Cygan et al. 2004; Zhou et al. 2020).

The studied temperature conditions were 300 K, 348 K, and 473 K, while pressure conditions were 0.1 MPa, 60 MPa, and 120 MPa. Thus, there were altogether 9 combinations of temperature and pressure conditions. The 300 – 473 K and 0.1 – 120 MPa ranges cover the most existence conditions of clay-rich gouge (Brown et al. 2017; Carpenter et al. 2012; Ikari et al. 2013; Lockner et al. 2011). Any temperature and pressure combination in this study is not referred to a specific geological setting, but rather serves to show the generic influence of pressure or temperature variation.

GROMACS 5.1 package (Hess et al. 2008) was used to perform simulations. The equation of motion was integrated with the leapfrog algorithm with a time step of 1.0 fs. A 7 ns isothermal-isobaric (NPT) simulation was performed with each dimension of the box scaled independently. Simulated annealing from 500 K to target temperature was performed during the first 2 ns, so as to well equilibrate structure. Berendsen thermostat and barostat (Berendsen et al. 1984) were used in this stage. Then, an $NP_\sigma T$ simulation, during which only the *z*-dimension of the box was scaled, was run for 70 - 150 ns. The Nosé-Hoover thermostat (Evans and Holian 1985; Hoover 1985; Nose 1984) and Parrinello-Rahman barostat (Parrinello and Rahman 1981) were used in this stage. Data were saved every 0.1 ps in the equilibrium $NP_\sigma T$

simulations. The coupled pressure in the z dimension (0.1 MPa, 60 MPa, and 120 MPa) is normal stress P_σ on the basal plane of smectite.

Bulk phase with 2165 water molecules, which mimic the pore fluid phase, was also simulated. An NPT simulation was performed for 18 ns. The same three temperature conditions (300 K, 348 K, and 473 K) were considered. At 300 K, the investigated pressures ranged from -120 MPa to 120 MPa with a gradient of 10 MPa except that 0 MPa was replaced by 0.1 MPa. At 348 K, because the bulk water phase blows up at -120 MPa, the pressure range was narrowed to be from -110 MPa to 120 MPa. At 473 K, the pressure range was from -40 MPa to 120 MPa. Simulated annealing from 500 K to target temperature was performed during the first 3 ns of an NPT simulation. Data were collected every 0.1 ps in the equilibrium NPT simulations. It is noted that water simulated here at all conditions is in the liquid state, as shown by the molecular volume of water (Section S1 in Supplemental Material), which is consistent with the liquid state description (Lopez-Lemus et al. 2008). The simulated water at some conditions (i.e., 473 K and negative pressure) is superheated liquid (Gallo et al. 2016), or in other words, in a metastable state. The stable state at such condtions is a vapor state or a vapor/liquid coexistence one. As we try to provide a generic insight on how the variation of temperature or pressure affects the coupling between pore and interlayer water, we do not simulate the stable state but rather the metastable one which maintains the liquid behavior. The coupled pressure of the bulk phase represents the pore fluid pressure P_f. In this study, we do not explicitly consider influence of solvated ions on the effective pore fluid pressure or osmotic pressure

(Kohns et al. 2016; Koop et al. 2000). In principle, chemical potential of bulk phase simulated here is equal to that of the real pore fluid with the same osmotic pressure P_f.

Figure 2

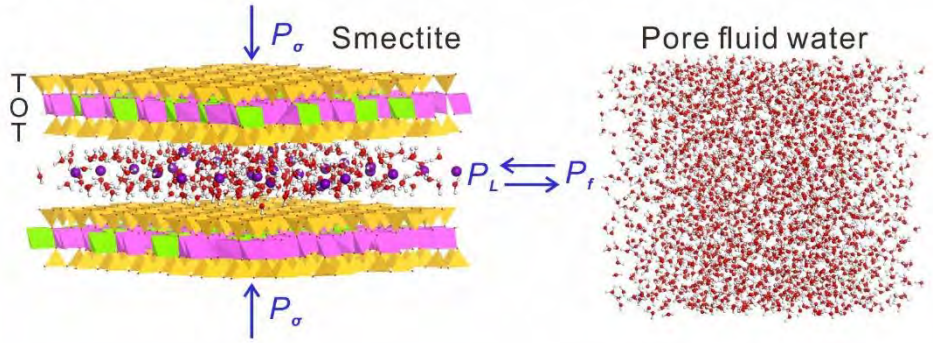

FIGURE 2. Schematic of water exchange between smectite interlayer and pore fluid. The TOT layer contains SiO_4 tetrahedron (yellow), AlO_6 octahedron (pink) and MgO_6 octahedron (fluorescent green). Water molecules (O atoms (red), H atoms (white)) and Na^+ ions (purple) are intercalated between layers.

Determination of stable hydration state of smectite

For water in smectite coupled with pore fluid (Fig. 2), we assumed no water flow between the two phases, i.e., a static condition. The static condition implied:

$$\mu_i = \mu_f \tag{3}$$

$$P_L = P_f \tag{4}$$

$$\Pi = P_\sigma - P_L \tag{5}$$

where μ_i and μ_f are chemical potentials of intercalated and pore fluid water, respectively, P_L is the lateral stress of water intercalated in smectite, and Π is the disjoining pressure which is the inherent property of intercalated water (Shchukin et al.

2001). If both smectite and pore fluid are under the same hydrostatic pressure, Eqs. (4) and (5) are derived to be $P_\sigma = P_L = P_f$ and $\Pi = 0$, as assumed in our previous study (Chen et al. 2020a). However, here we are interested in the mechanical non-equilibrium state with $P_\sigma \neq P_f$. We express the hydration Gibbs free energy G_{hyd} as a function of the interlayer spacing l:

$$G_{\mathrm{hyd}}(l) = -A\int_0^l \Pi(l)\,dl' + \left(P_\sigma - P_f\right)\cdot A\cdot l \tag{6}$$

in which the former term accounts for the work done by intercalated water, while the latter accounts for that by environment. A is the area of a basal surface. The minimum of $G_{\mathrm{hyd}}(l)$ corresponds to the static state. Alternatively, G_{hyd} can be seen as a function of the number of intercalated water molecules (N):

$$G_{\mathrm{hyd}}(N) = \int_0^N \left[\mu_i(N, P_\sigma) - \mu_f(P_f)\right] dN' \tag{7}$$

μ_i and μ_f at certain temperature and pressure conditions are derived with TI through decoupling interactions between a water molecule and surrounding environment, which can be found in our previous studies (Chen et al. 2020a; Chen et al. 2020b; Zhou et al. 2020) and briefly introduced in Section S2 of the Supplemental Material.

In this study, we derive $\mu_i(N)$ and μ_f at conditions (P_σ = 0.1 MPa, T = 300 K), (P_σ = 60 MPa, T = 348 K), and (P_σ = 60 MPa, T = 473 K) through decoupling interactions. $\mu_i(N)$ under the same T but different P_σ conditions can be derived by the following integration:

$$\mu_i\left(N, P_{\sigma,j}, T\right) - \mu_i\left(N, P_{\sigma,i}, T\right) = \int_{P_{\sigma,i}}^{P_{\sigma,j}} \left(\frac{\partial V}{\partial N}\right)_{N,P'_\sigma,T} dP'_\sigma \tag{8}$$

in which $\left(\frac{\partial V}{\partial N}\right)_{N,P'_\sigma,T}$ is the partial derivative of volume with N, as derived with equilibrium configurations with various N (Chen et al. 2020a). If $P_{\sigma,j}$ is close to $P_{\sigma,i}$

and the variation of $\left(\frac{\partial V}{\partial N}\right)_{N,P'_{\sigma},T}$ with P_{σ}' is small, the chemical potential difference can be approximated as:

$$\mu_i(N, P_{\sigma,j}, T) - \mu_i(N, P_{\sigma,i}, T) \approx \frac{P_{\sigma,j} - P_{\sigma,i}}{2} \cdot \left[\left(\frac{\partial V}{\partial N}\right)_{N,P_{\sigma,i},T} + \left(\frac{\partial V}{\partial N}\right)_{N,P_{\sigma,j},T}\right] \quad (9)$$

With Eq. (9), we derive μ_i (N) under all the studied pressure conditions.

As to μ_f, the dependence of it on pressure is similarly:

$$\mu_f(P_{f,j}, T) - \mu_f(P_{f,i}, T) = \int_{P_{f,i}}^{P_{f,j}} V_f(P'_f, T) dP'_f \quad (10)$$

where V_f is the molecular volume of pore fluid water (bulk water here). Equilibrium data of V_f at discrete P_f' conditions are recorded (Section S1 in Supplemental Material). Through fitting the data with a third-order polynomial equation, we derive the $V_f(P_f')$ function. Substituting the function into Eq. (10), with the known $\mu_f(P_{f,i}, T)$ derived with TI, $\mu_f(P_{f,j}, T)$ is achieved. With μ_i and μ_f and Eq. (7) we get $G_{\mathrm{hyd}}(N)$. $G_{\mathrm{hyd}}(N)$ is transformed into $G_{\mathrm{hyd}}(n)$, in which n is water content in the chemical formula of smectite. n at the minimum of G_{hyd} corresponds to the stable hydration state of smectite under conditions characterized by P_{σ}, P_f, and T.

Non-equilibrium molecular dynamics simulations

The equilibrium configuration of a stable hydration state at a condition (P_{σ}, P_f, and T) was used to initiate a NEMD simulation in an $NP_{\sigma}T$ ensemble. The two TOT layers and water intercalated between them in the middle of the smectite model are seen as one group, referred to as a pulled group (Fig. 3a). A linear potential parallel with the basal plane was added to the pulled group. Thus, the pulled group was in a field like a gravitational field and therefore a constant force (***F***) was at the center of mass of the

group. ***F*** does not vary with the number of atoms in the pulled group. A large enough ***F*** would lead to dislocation between layers. In a steady state, the friction force is equal to F. The shear stress is expressed as:

$$\tau = \frac{F}{2A} \tag{11}$$

where A is the area of a basal surface. Because the pulled group was in contact with two basal surfaces, the denominator in Eq. (11) was $2A$. In this study, ***F*** along directions x, $-x$, y, and $-y$ were adopted (Fig. 3b). Thus, we denote τ as τ_x, τ_{-x}, τ_y, and τ_{-y}, whose subscripts represent pull directions.

Figure 3

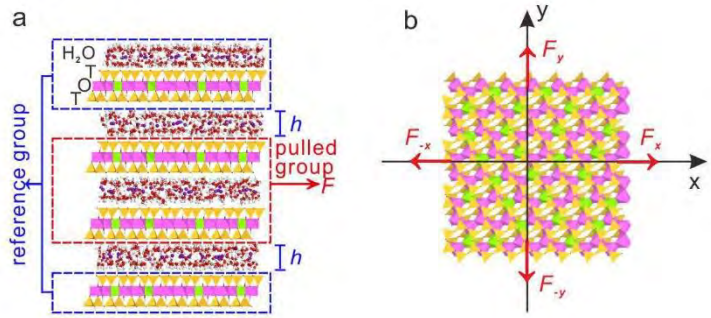

FIGURE 3. Schematic of NEMD simulation model: (a) side view; (b) top view. Color representations are the same as those in Fig. 2.

A NEMD simulation lasted for 1-6 ns. The simulation time depended on how long it took for the pulled group to reach a steady state. The topmost and downmost TOT layers and water molecules between them across the periodic boundary are seen as the reference group (Fig. 3a), whose center of mass was kept fixed during a simulation. At a condition, a series of NEMD simulations with different ***F*** on the pulled group

were performed. The displacement of the pulled group with time is recorded.

Because how the thermostat is applied could affect NEMD simulation result (de Wijn and Pettersson 2017), we tried two thermostating ways: I. Separate thermostat: we separated two thermostating groups, one was the reference group, and the other was the pulled group and the two water layers beneath or above it. These two groups were separately thermostated, so that heat generated by frictional sliding would be removed; II. Partial thermostat: only the reference group was thermostated, so that it allowed local temperature increase due to heat generated by frictional sliding. With these two thermostating methods, whether the frictional heat has an influence on sliding would be shown.

RESULTS

Hydration state of smectite at different P_σ, P_f, and T conditions

At a condition characterized by P_σ, P_f, and T, the global minimum of $G_{\mathrm{hyd}}(n)$ is referred to the stable hydration state of smectite (Fig. 4). At conditions when P_f is high enough, there is no global free energy minimum in $G_{\mathrm{hyd}}(n)$. In these cases, when n is larger than some value, $G_{\mathrm{hyd}}(n)$ decreases monotonically as n increases. Thus, layer-by-layer stacking smectite is not available at these conditions, and exfoliation of smectite is anticipated.

This is the peer-reviewed, final accepted version for American Mineralogist, published by the Mineralogical Society of America.
The published version is subject to change. Cite as Authors (Year) Title. American Mineralogist, in press.
DOI: https://doi.org/10.2138/am-2022-8195. http://www.minsocam.org/

Figure 4

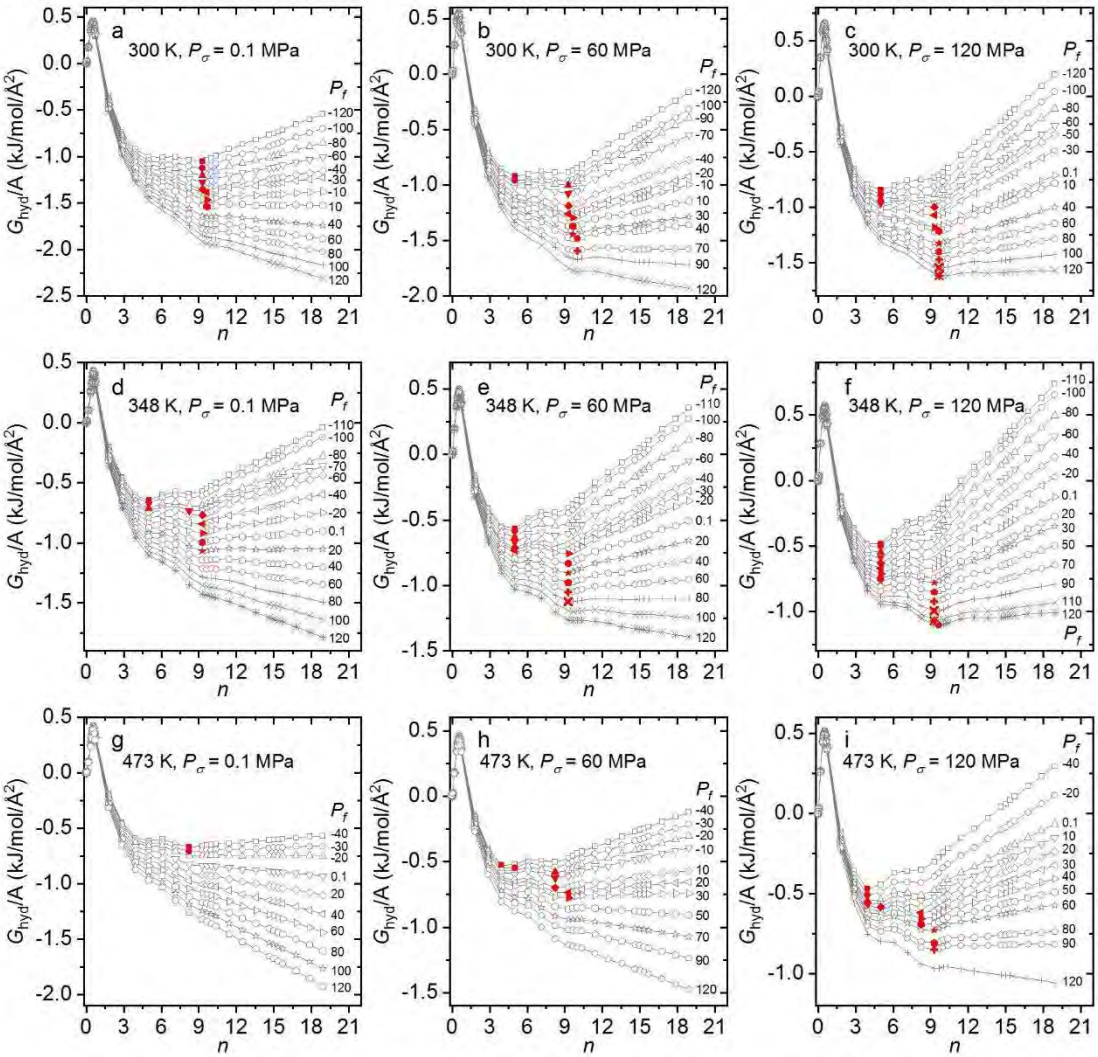

FIGURE. 4. Hydration Gibbs free energy G_{hyd} normalized by basal surface area A as a function of water content n. Results at different temperatures and normal stresses are shown in different panels. In each panel, different free energy curves refer to cases with different pore fluid pressures. The global free energy minimum is denoted by a red symbol.

We compile n referring to global minima at different conditions and show them in Fig. 5. There are roughly two hydration states of smectite, one with n less than 6.0, and the other with n larger than 8.0. Water in the former state roughly exhibits a monolayer form (Fig. 5d), while water in the latter appears as a bilayer (Fig. 5e).

These water arrangements are consistent with previous studies (Mazo et al. 2008; Zhang et al. 2014; Zhou et al. 2020). We refer to the two states as 1W and 2W, respectively, in consistent with previous designation (Ferrage 2016). At a P_σ and T condition, the increase of P_f generally induces the transformation from a 1W state to a 2W one. At the same temperature, when P_σ is higher, it requires a higher P_f to transform smectite from a 1W state to a 2W one (Fig. 5a-c). At the condition T = 300 K and P_σ = 0.1 MPa, only a 2W state is available under the studied range of pore fluid pressure (Fig. 4a, Fig. 5a), the same as that at the condition T = 473 K and P_σ = 0.1 MPa (Fig. 4g, Fig. 5c).

Figure 5

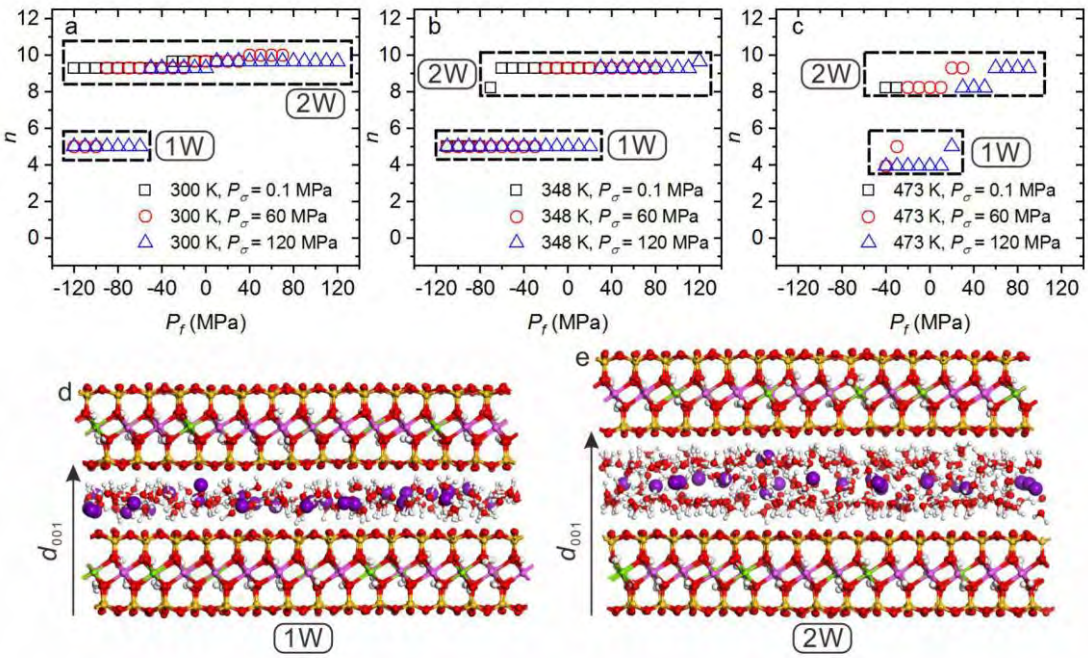

FIGURE. 5. The stable water content (n) of smectite as a function of pore fluid pressure (P_f) in cases at different temperatures (T) and normal stresses (P_σ) (a-c). Snapshots of monolayer (1W) and bilayer (2W) hydration states are shown (d, e). Color representations are the same as those in

Fig. 1.

Simulated interlayer sliding of smectite

With stable hydration states of smectite at different P_σ, P_f, and T conditions, NEMD simulations were performed to show sliding between layers. The displacement of the pulled layers with time is shown in Fig. 6. When $\boldsymbol{F}$ is too small, the pulled group is stationary in the steady state (Fig. 6a,d). As $\boldsymbol{F}$ increases, the pulled group exhibits a stepwise movement (Fig. 6b,e). When $\boldsymbol{F}$ is large, a linear displacement (s) with time (t) is observed (Fig. 6c,f). Through linear fitting of $s(t)$ in the steady state (Fig. 6), we derive the slope of $s(t)$, which is the velocity component along x, $-x$, y, and $-y$ directions. The direction of $\boldsymbol{v}$ is not necessarily along the pull direction, as a small nonzero velocity component perpendicular to it is observed (Fig. S2-S7 in Supplemental Material). In the following, we just refer to the magnitude of $\boldsymbol{v}$.

This is the peer-reviewed, final accepted version for American Mineralogist, published by the Mineralogical Society of America.
The published version is subject to change. Cite as Authors (Year) Title. American Mineralogist, in press.
DOI: https://doi.org/10.2138/am-2022-8195. http://www.minsocam.org/

Figure 6

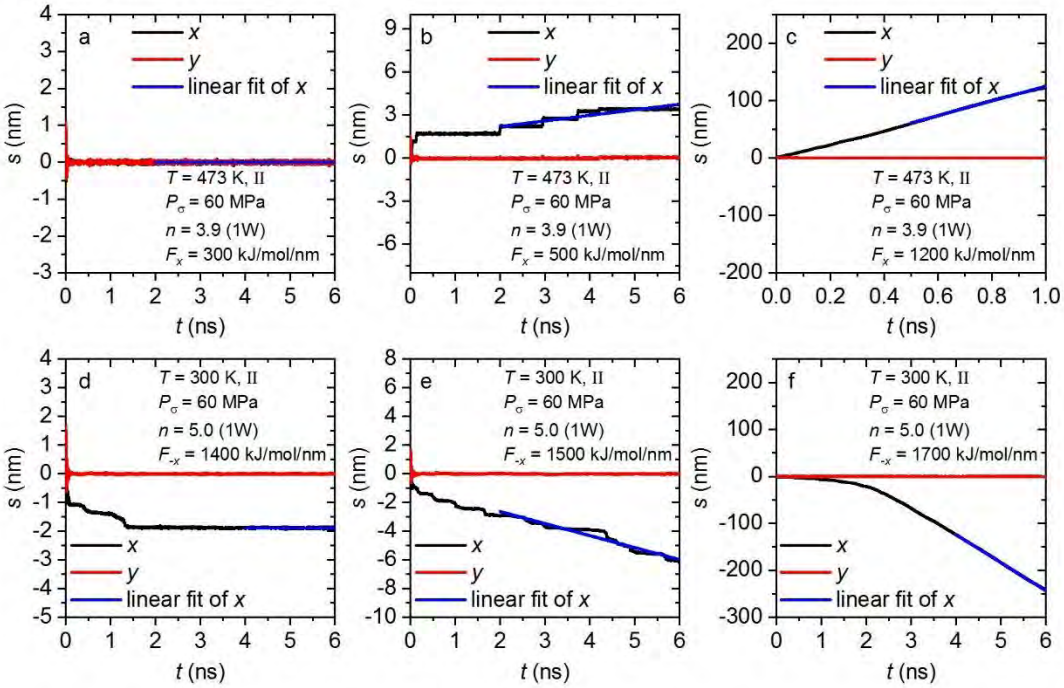

FIGURE 6. Displacement (s) of the pulled group as a function of time (t). x and y denote displacement components along x and y coordinates, respectively. A constant force $\boldsymbol{F}$ which is along x or $-x$ direction is exerted on the pulled group. Linear fit of the displacement component along the x coordinate in the steady state is shown. "II" denotes that partial thermostat was used.

In the steady state, velocity of water next to the pulled layer is statistically the same as the steady-state velocity of that layer. At the same time, water next to the reference layer almost does not flow. An example of the distribution of the steady-state water velocity is shown in Fig. 7.

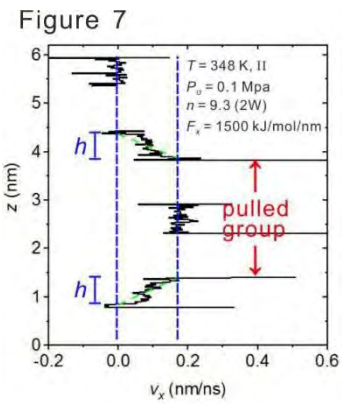

FIGURE 7. Velocity profile of water in the steady state. The bule dash lines mark velocities of the pulled and stationary layers. The green dash line shows the linear fit to the velocity profile of water.

Shear response of smectite interlayer

The relationships between shear stress and velocity magnitude are shown in Fig. 8 (results with partial thermostat) and Fig. S8 in Supplemental Material (results with separate thermostat). For steady slidings, τ increases with steady-state velocity v, corresponding to a velocity-strengthening behavior. However, we find that τ does not scale with ln v, i.e., the interlayer sliding does not follow the form of the RSF law. Instead, a log-log scaling between τ and v is found. $\tau(v)$ can be phenomenologically fitted with the following equation:

$$\ln \tau = k \ln v + \ln \tau_i \tag{12}$$

where τ_i and k are defined as initial shear stress and velocity-strengthening constant here. In results with either thermostat, Eq. (12) well fits most data (Fig. 8 and Fig. S8 in Supplemental Material). The log-log plots in Fig. S9 and S10 in Supplemental Material clearly show the general well fittings. However, in some cases (1W state

with T = 300 K and P_σ = 60 or 120 MPa; 2W state with T = 300 K and P_σ = 120 MPa), a discontinuous jump of v with τ is observed (Fig. 8a,b,h and Fig. S8a,b,h in Supplemental Material). This is reminiscent of the stick-slip regime when a surface is driven with a spring at a constant velocity, which probably implies a dynamic phase transition (Drummond and Israelachvili 2001; Urbakh et al. 2004). Here, the pulled group remains stationary until τ reaches a threshold. Equilibrium trajectories of the stationary state show that an intercalated water molecule vibrates but almost does not diffuse (Supplemental Videos). It is an ice-like structure (Chen et al. 2020a; Leng and Cummings 2006). When τ is smaller than the threshold, a snapshot shows a hydrogen bond (HB) network is well developed among water molecules (Fig. 9a). When τ is larger than the threshold, the HB network is largely broken (Fig. 9b), corresponding to a first-order phase transition. We calculate the number of HBs per water molecule forms (N_{HB}), with the HB criterion: the donor−acceptor distance, the hydrogen−acceptor distance, and the hydrogen−donor−acceptor angle are less than 0.35 nm, 0.245 nm, and 30°, respectively (Laage and Hynes 2006; 2008). As τ increases, we observe a discontinuous drop of N_{HB} (Fig. 9c). The radial distribution function ($g(r)$) between water O atoms also shows a discontinuous structural variation (Fig. 9d). They evidence a shear-induced ice-like to liquid-like phase transition. In other cases where v continuously increases with τ (Fig. 8 and Fig. S8 in Supplemental Material), no distinct structural variation happens as shown by N_{HB} (Fig. 9c) and $g(r)$ (Fig. 9d). Good fitting with Eq. (12) implies even a small non-zero τ could initiate an interlayer slip given that simulation time was as long as possible. In addition, for the

1W state at 473 K with P_σ = 60 or 120 MPa, Eq. (12) well fits low velocity data, but it deviates from high velocity ones (Fig. 8o,p and Fig. S8o,p in Supplemental Material). This state is characterized by a relatively lower water content (n = 3.9). The deviation from a simple log-log scaling probably implies a multiple-stage sliding dynamics but without phase transition. Based on the log-log plots in Fig. S9 and S10 in Supplemental Material, when v is as small as less than 10 nm/ns, a deviation from the log-log plot is observed. This can also be explained as multiple-stage sliding dynamics. Nevertheless, the deviation of the magnitude of τ from the log-log plot is just small in such a low velocity regime.

This is the peer-reviewed, final accepted version for American Mineralogist, published by the Mineralogical Society of America.
The published version is subject to change. Cite as Authors (Year) Title. American Mineralogist, in press.
DOI: https://doi.org/10.2138/am-2022-8195. http://www.minsocam.org/

Figure 8

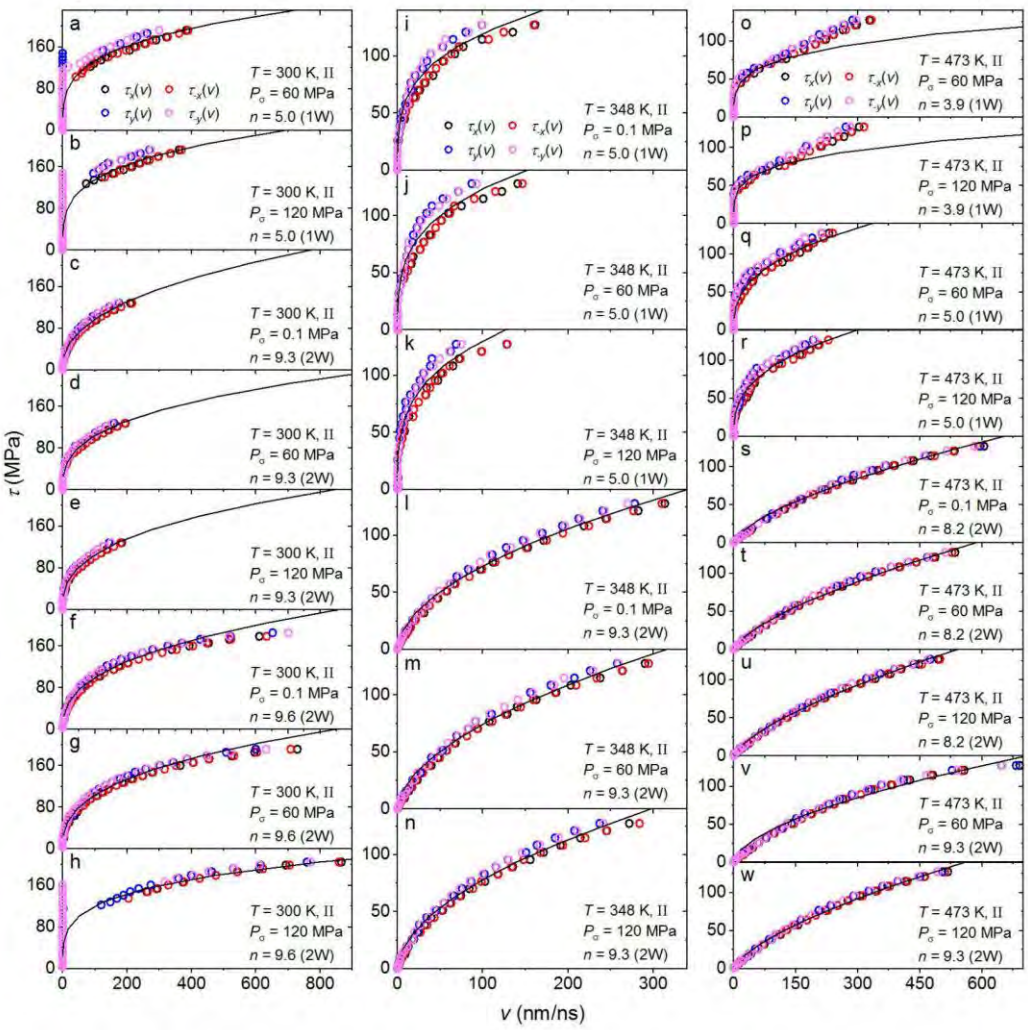

FIGURE 8. Shear stress (τ) as a function of velocity magnitude (v) of the pulled group at 300 K (left), 348 K (middle), and 473 K (right). Subscripts (x, $-x$, y, and $-y$) denote directions of the shear stress. Fittings with Eq. (12) are shown. "II" denotes that partial thermostat was used.

This is the peer-reviewed, final accepted version for American Mineralogist, published by the Mineralogical Society of America.
The published version is subject to change. Cite as Authors (Year) Title. American Mineralogist, in press.
DOI: https://doi.org/10.2138/am-2022-8195. http://www.minsocam.org/

Figure 9

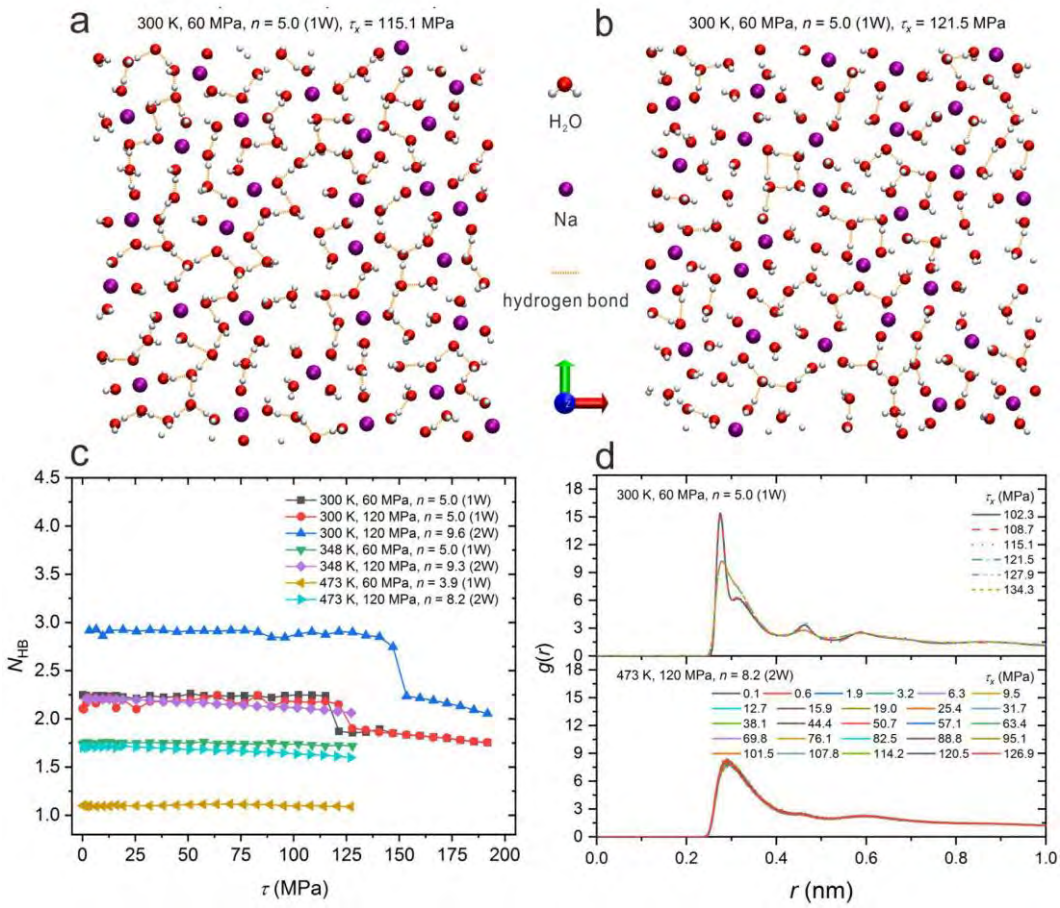

FIGURE 9. Structure of water in the interlayer of smectite. Panels (a) and (b) show top-view configurations of water before and after a shear-induced phase transition, respectively. Panel (c) shows number of hydrogen bonds (N_{HB}) per water molecule forms as a function of shear stress. Panel (d) shows the radial distribution function between water O atoms. These results were derived with partial thermostat.

DISCUSSION

Comparison between simulations and laboratory friction experiments

The shear velocity magnitude reported here is of the order of nm/ns (i.e., m/s), but that reported in laboratory friction experiment is much smaller and of the order of μm/s (Carpenter et al. 2012; Diao and Espinosa-Marzal 2018; Ikari et al. 2013). In

most cases we studied here, the log-log scaling between τ and v (Fig. 8) implies that even a small finite τ can induce an interlayer slip. Given that simulation time was as long as possible, a stepwise movement of the pulled layer under a finite τ like those in Fig. 6b,e is anticipated. However, due to the limitation of the current computational powers, reproducing such a low shear velocity as those in laboratory experiments is impossible. Nevertheless, in cases without dynamic phase transition, the log-log scaling between τ and v could be extrapolated to the lower velocity regime. It provides an estimate of the relationship between τ and v. In cases with dynamic phase transitions, the threshold value of τ which induces a transition and the initiate shear velocity are hard to be determined as it takes long enough simulations to guarantee the reliability. In those cases, the shear dislocation between clay layers is harder to be induced.

Diao and Espinosa-Marzal (2018) slided a silica tip along a calcite surface in aqueous solution with atomic force microscopy (AFM) to produce a shear rate of the order of μm/s with a shear stress of the order of Pa. However, the shear experiment on fault gouge produces the same order of a shear rate of the amorphous solid with a shear stress of a much higher order of MPa (Collettini et al. 2019). This discrepancy reflects that, the macroscopic shear displacement is different from the microscopic one. If the AFM tip was under a shear stress of the same order as in shear experiments on fault gouge, a shear rate of a much higher order is anticipated. We use the concept of hot spots (Amon et al. 2012; Pons et al. 2016) to refer to sites in amorphous solid which are more susceptible to plastic deformations. Those sites could be grain

boundaries intercalated by water or clay interlayers. Under an applied macroscopic shear stress, the local shear rates in hot spots are higher than the macroscopic one. Because shear sliding between clay layers is velocity-strengthening, the sliding would stop and the stress in hot spots would be released and propagated to environmental sites. In this study we show that under a shear stress of the order of MPa (the same order as in shear experiments on fault gouge) the shear rate between clay layers is of the high order of m/s, which evidences the role of clay layers as hot spots.

Origin of the shear response of smectite interlayer

Diao and Espinosa-Marzal (2018) found a log-log scaling between friction force and velocity in the AFM experiment. The log-log scaling between τ and v might be common when an aqueous layer is confined between sliding surfaces. Such a scaling is reminiscent of shear flow of non-Newtonian fluid, which can be described by the Ostwald de Waele equation (Chhabra 2010):

$$\tau = m\left(\frac{v}{h}\right)^k \tag{13}$$

where m and k are constants and h is the fluid thickness. Eq. (13) can be transformed into Eq. (12) with $\ln \tau_i = \ln m - k \ln h$. Thus, the log-log scaling between τ and v is in fact derived from the Ostwald de Waele equation which describes shear fluid flow. The shear flow is manifested by an approximately linear distribution of water velocity with distance (Fig. 7). Thus, the shear rate (v/h) under a shear stress (τ) is controlled by viscosity (η) of interlayer water (Landau and Lifschitz 1987):

$$v/h = \frac{\tau}{\eta} \tag{14}$$

Combining Eqs. (13) and (14), η can be derived with the following equation:

$$\eta = m\left(\frac{v}{h}\right)^{k-1} \tag{15}$$

We show the relationship between η and v/h in Fig. 10 and Fig. S11 in Supplemental Material. The function line of Eq. (15) is also presented according to $m = \exp(\ln \tau_i + k \ln h)$ and with the fitted values of τ_i and k (Fig. 8 and Fig. S8 in Supplemental Material). Fig. 10 shows Eq. (15) generally explains the log-log scaling between η and v/h. η decreases with shear rate, which implies interlayer water is a shear-thinning fluid (Hartkamp et al. 2013; Leng and Cummings 2005; Thompson et al. 1995). Shear thinning appears when the structural relaxation rate of fluid is smaller than the shear rate (Leng and Cummings 2005).

The viscosity response to shear rate is the intrinsic property of interlayer water, which explains log-log scaling between τ and v and the velocity-strengthening behavior. Different viscosities of water in 1W and 2W states and variations with shear rate give rise to different shear responses. The phenomenological RSF law with a form of a $\tau \sim \ln v$ scaling (Baumberger and Caroli 2006; Kawamura et al. 2012; Scholz 1998) is not applicable for the viscous shear between clay layers. For sliding between solid surfaces with water as lubricant, experiments have found a $\tau \sim \ln v$ or a $\ln \tau \sim \ln v$ scaling (Diao and Espinosa-Marzal 2018; Ma et al. 2015). The $\tau \sim \ln v$ relation was found in the low hydration regime. In this regime, hydrated ions at the surface act as asperity contacts, so that dislocation between surfaces is an activated process requiring crossing of an energy barrier. However, even for the 1W hydration state studied here, shear between layers follows a $\ln \tau \sim \ln v$ relation. Snapshots show

ions are not present as asperities (Fig. 5d,e) but flow with water. The viscous flow of water supports the ln $\tau \sim$ ln v relation. As for the interlayer with ice-like water, a slide only begins after a dynamic phase transition, which is an activated process. Thus, if a statistical analysis was on a clay matrix which consists of many interlayers with ice-like water, the deformation of the matrix may follow the $\tau \sim$ ln v relation. This scenario appears at a high pressure but close to ambient temperature condition.

Figure 10

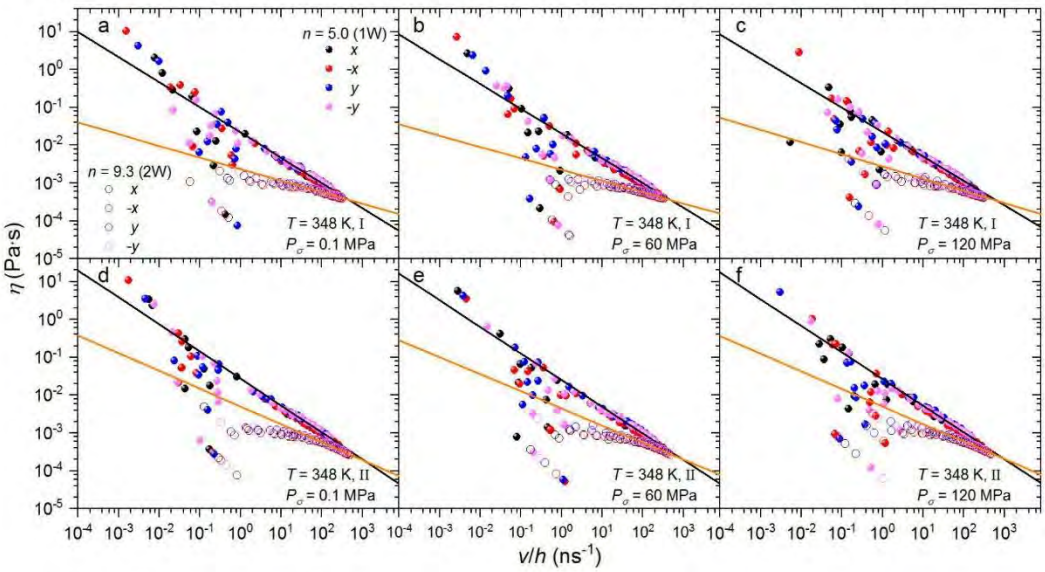

FIGURE 10. The effective viscosity (η) as a function of shear rate (v/h) at 348 K with separate (I) (a,b,c) and partial (II) thermostats (d,e,f). Solid lines are function lines of Eq. (15) derived with fitted values of τ_i and k. Black and yellow lines correspond to results of the 1W and 2W states, respectively.

Effects of P_σ, P_f, and T on shear strength and its velocity dependence

Through fitting $\tau(v)$ (Fig. 8) we derive τ_i and k, which are dynamic characteristics of interlayer water with a fixed content under conditions of T and P_σ. τ_i is the shear

stress at a low sliding velocity. It is noted that τ_i is not the yield shear stress, because when interlayer water is in a fluidic state, steady sliding is always available only if τ is non-zero. When interlayer water is in an ice-like state under low shear stress, the fitted τ_i is smaller than the threshold stress which induces a phase transition. As shown in the thermodynamic analysis, the variation of effective normal stress ($\Delta P = P_\sigma - P_f$) can lead to alternation of a hydration state, which in turn changes τ_i. We show τ_i as a function of ΔP in Fig. 11. The error bar of ΔP refers to the range of P_f in which the hydration state of smectite does not change (Fig. 5a-c). According to Eq. (1), with τ_i and ΔP, friction coefficient μ_d can be derived in principle. However, the variation of τ_i with ΔP in an isothermal condition is stepwise (Fig. 11). When interlayer water is in a fluidic state, if ΔP is increased but the hydration state is not changed, the variation of τ_i is almost negligible. The alternation of a hydration state due to increased ΔP leads to a sharp increase of τ_i. Due to the non-linear relation between τ_i and ΔP, the Amontons' law breaks down here. Linear fitting of $\tau_i(\Delta P)$ would result in an apparent friction coefficient not larger than 0.3, as guided by the $\tau_i = 0.3\Delta P$ line in Fig. 11. Laboratory experimental studies have shown that clay-rich samples exhibit a macroscopic friction as low as $0.1 < \mu_d < 0.3$ (Collettini et al. 2019). Thus, this study here discloses the low macroscopic friction strength can be attributed to the shear displacement between smectite layers.

This is the peer-reviewed, final accepted version for American Mineralogist, published by the Mineralogical Society of America.
The published version is subject to change. Cite as Authors (Year) Title. American Mineralogist, in press.
DOI: https://doi.org/10.2138/am-2022-8195. http://www.minsocam.org/

Figure 11

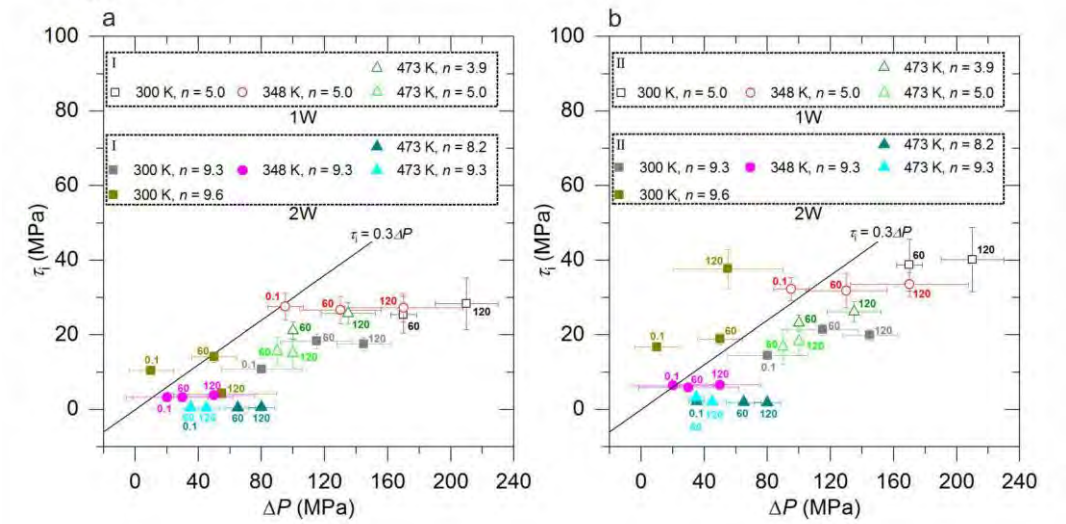

FIGURE 11. The initial shear stress (τ_i) as a function of the effective normal stress (ΔP). Panels (a) and (b) show results with separate (I) and partial (II) thermostats, respectively. The number marked next to the symbol is the P_σ value whose unit is MPa. The function line of $\tau_i = 0.3\Delta P$ is shown to guide the upper bound of the friction coefficient.

It is noted that even for samples rich in phyllosilicate minerals without intercalated water, the macroscopic friction still fulfill the range $0.1 < \mu_d < 0.3$ (Collettini et al. 2019). Thus, the low friction coefficient is not exclusively determined by intercalated water. If the variation of ΔP is too small to induce a transition between different hydration states of smectite, the alternation of τ_i is almost negligible (Fig. 11) and μ_d would be approaching 0. Thus, the major mechanical difference between clay minerals in different hydration states is not μ_d but τ_i, which quantifies the ability as hot spots. τ_i for the 2W state is generally smaller than that for the 1W one (Fig. 11), as viscosity of interlayer water in the 2W state is smaller (Fig. 10).

As temperature increases, for the same hydration state, τ_i generally decreases, due

to decrease of viscosity. When temperature is constant, if the hydration state does not change, increasing ΔP generally does not lead to a considerable variation of τ_i, except in case increased ΔP leads to a phase transition, e.g., 2W state at 300 K transforms from a fluidic state to an ice-like one from 60 to 120 MPa. However, τ_i of the ice-like state is meaningless as it is much smaller than the yield stress.

At the same temperature, k for the 2W state is generally larger than that for the 1W state (Fig. 12), implying velocity-strengthening friction is elevated. It can be explained by the viscosity of interlayer water in the 2W state which decreases less with shear rate (Fig. 10). For the 2W state, temperature increase generally leads to the enlargement of k, but it is not clear for the 1W state, as also explained by the viscosity variation. When temperature is unchanged, variation of ΔP without changing the hydration state does not lead to a considerable variation of k.

Figure 12

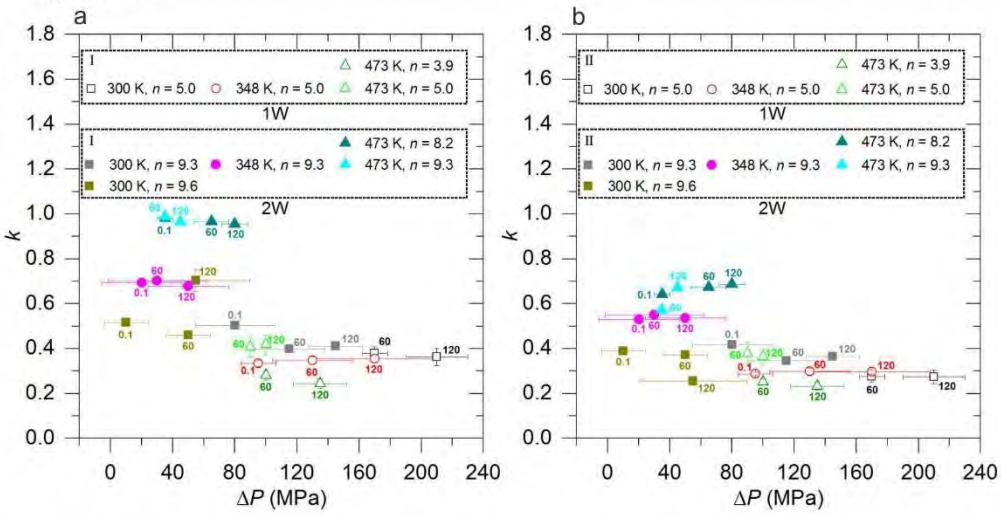

FIGURE 12. The velocity-strengthening constant (k) as a function of the effective normal stress (ΔP). Panels (a) and (b) show results with separate (I) and partial (II) thermostats, respectively.

The number marked next to the symbol is the P_σ value whose unit is MPa.

We provide the first mechanistic insight on how delamination between clay layers supports aseismic slip. The interlayer water lubricant gives rise to a velocity-strengthening behavior, as interlayer water is a viscous fluid. Interlayer water is a shear-thinning fluid, whose viscosity response to shear rate determines the relationship between shear stress and velocity. The variation of temperature, normal stress, or pore fluid pressure alters hydration state of an interlayer, and thus it causes changes of dynamic characteristics. Viscosity of the 2W hydration state is lower than that of the 1W one, which results in the lower frictional resistance. The velocity-strengthening behavior is more significant for the 2W state, due to less decrement of viscosity with shear rate. Thus, clay minerals in the 2W hydration state are more prone to act as hot spots.

We think separate thermostat gives rise to a more accurate estimation of τ_i, but with partial thermostat k is better estimated. With partial thermostat, frictional sliding accompanies heat generation, which implies energy dissipation. As a result, the increment of v requires a larger increment of τ than in case with separate thermostat. Thus, k for the 2W state simulated with partial thermostat is lower (Fig. 12b). As heat generation is also anticipated when sliding natural samples, we think the partial thermostat better estimates k. On the other hand, when sliding has not happened or sliding is very weak, energy dissipation into environment is fast. Thus, separate thermostat is more reasonable as temperature is consistent with environment. τ_i is the

stress at a low shear rate, so that it is better derived with the separate thermostat. Thus, Fig. 11a and Fig. 12b are recommended estimations of initial shear stress and velocity-strengthening ability, respectively.

IMPLICATIONS

Properties of minerals primarily determine fault mechanics. The viscous deformation of serpentine antigorite at high pressure impedes stress buildup and supports interseismic creep (Hilairet et al. 2007). Similarly, the viscous shear between clay layers shown here supports aseismic slip. Shear behavior of smectite does not monotonically vary with pressure or temperature, but the alternation of a hydration state with environment plays a key role. We suggest that disclosing the hydration state of a clay mineral is preliminary. Understanding local slip between clay layers paves the way for uncovering the constitutive law to describe fault gouge deformation. In this work we verify the role of clay minerals as hot spots which support aseismic slip, but future numerical studies would be needed to connect the local plastic deformation in clay layers and macroscopic fault dynamics.

Acknowledgements

This work was financially supported by National Natural Science Foundation of China (41825003, 41921003), Key Research Program of Frontier Sciences, Chinese Academy of Sciences (CAS) (QYZDJ-SSW-DQC023), CAS Interdisciplinary Innovation Team (JCTD-2019-15), Science and Technology Planning of Guangdong

Province, China (2020B1212060055), and Youth Innovation Promotion Association CAS (2019345). We are grateful to the National Supercomputer Center in Guangzhou for the use of the high-performance computing facility.

References

Amon, A., Nguyen, V.B., Bruand, A., Crassous, J., and Clément, E. (2012) Hot spots in an athermal system, Physical Review Letters. 108(13), 135502.

Aretusini, S., Plumper, O., Spagnuolo, E., and Di Toro, G. (2019) Subseismic to seismic slip in smectite clay nanofoliation, Journal of Geophysical Research-Solid Earth. 124(7), 6589-6601.

Avouac, J.-P. (2015) From geodetic imaging of seismic and aseismic fault slip to dynamic modeling of the seismic cycle, Annual Review of Earth and Planetary Sciences. 43, 233-271.

Baumberger, T., and Caroli, C. (2006) Solid friction from stick–slip down to pinning and aging, Advances in Physics. 55(3-4), 279-348.

Berendsen, H.J.C., Grigera, J.R., and Straatsma, T.P. (1987) The missing term in effective pair potentials, Journal of Physical Chemistry. 91(24), 6269-6271.

Berendsen, H.J.C., Postma, J.P.M., Vangunsteren, W.F., Dinola, A., and Haak, J.R. (1984) Molecular-dynamics with coupling to an external bath, Journal of Chemical Physics. 81(8), 3684-3690.

Brown, K.M., et al. (2017) The action of water films at Å-scales in the earth: Implications for the nankai subduction system, Earth and Planetary Science Letters. 463, 266-276.

Bürgmann, R., Schmidt, D., Nadeau, R.M., d'Alessio, M., Fielding, E., Manaker, D., McEvilly, T.V., and Murray, M.H. (2000) Earthquake potential along the northern hayward fault, california, Science. 289(5482), 1178-1182.

Carlson, J.M., Langer, J.S., and Shaw, B.E. (1994) Dynamics of earthquake faults, Reviews of Modern Physics. 66(2), 657-670.

Carpenter, B.M., Saffer, D.M., and Marone, C. (2012) Frictional properties and sliding stability of the san andreas fault from deep drill core, Geology. 40(8), 759-762.

Chen, M., Zhou, H., Zhu, R., and He, H. (2020a) Pressure-temperature diagram of wetting and dewetting in a hydrophobic grain boundary and the liquidlike to icelike transition of monolayer water, Physical Review B. 101(16)

Chen, M., Zhou, H., Zhu, R., Lu, X., and He, H. (2020b) Closest-packing water monolayer stably intercalated in phyllosilicate minerals under high pressure, Langmuir. 36(2), 618-627.

Chen, W., Foster, A.S., Alava, M.J., and Laurson, L. (2015) Stick-slip control in nanoscale boundary lubrication by surface wettability, Physical Review Letters. 114(9), 095502.

Chhabra, R.P. (2010) *Non-newtonian fluids: An introduction*, Springer, New York.

Collettini, C., Tesei, T., Scuderi, M.M., Carpenter, B.M., and Viti, C. (2019) Beyond byerlee friction, weak faults and implications for slip behavior, Earth and Planetary Science Letters. 519, 245-263.

Cygan, R.T., Liang, J.J., and Kalinichev, A.G. (2004) Molecular models of hydroxide, oxyhydroxide, and clay phases and the development of a general force field, Journal of Physical Chemistry B. 108(4), 1255-1266.

Darden, T., York, D., and Pedersen, L. (1993) Particle mesh ewald - an n.Log(n) method for ewald sums in large systems, Journal of Chemical Physics. 98(12), 10089-10092.

de Wijn, A.S., and Pettersson, L.G.M. (2017) How square ice helps lubrication, Physical Review B. 95(16), 8.

Dhopatkar, N., Defante, A.P., and Dhinojwala, A. (2016) Ice-like water supports hydration forces and eases sliding friction, Science Advances. 2(8), e1600763.

Di Toro, G., Goldsby, D.L., and Tullis, T.E. (2004) Friction falls towards zero in quartz rock as slip velocity approaches seismic rates, Nature. 427(6973), 436-439.

Diao, Y., and Espinosa-Marzal, R.M. (2018) The role of water in fault lubrication, Nature Communications. 9

Drummond, C., and Israelachvili, J. (2001) Dynamic phase transitions in confined lubricant fluids under shear, Physical Review E. 63(4), 041506.

Essmann, U., Perera, L., Berkowitz, M.L., Darden, T., Lee, H., and Pedersen, L.G. (1995) A smooth particle mesh ewald method, Journal of Chemical Physics. 103(19), 8577-8593.

Evans, D.J., and Holian, B.L. (1985) The nose-hoover thermostat, Journal of Chemical Physics. 83(8), 4069-4074.

Ferrage, E. (2016) Investigation of the interlayer organization of water and ions in smectite from the combined use of diffraction experiments and molecular simulations. A review of methodology, applications, and perspectives, Clays and Clay Minerals. 64(4), 348-373.

French, M.E., Chester, F.M., and Chester, J.S. (2015) Micromechanisms of creep in clay-rich gouge from the central deforming zone of the san andreas fault, Journal of Geophysical Research-Solid Earth. 120(2), 827-849.

Gallo, P., et al. (2016) Water: A tale of two liquids, Chemical Reviews. 116(13), 7463-7500.

Handin, J. (1969) On coulomb-mohr failure criterion, Journal of Geophysical Research. 74(22), 5343-&.

Hartkamp, R., Todd, B.D., and Luding, S. (2013) A constitutive framework for the non-newtonian pressure tensor of a simple fluid under planar flows, The Journal of Chemical Physics. 138(24), 244508.

Hensen, E.J.M., Tambach, T.J., Bliek, A., and Smit, B. (2001) Adsorption isotherms of water in li-, na-, and k-montmorillonite by molecular simulation, Journal of Chemical Physics. 115(7), 3322-3329.

Heslot, F., Baumberger, T., Perrin, B., Caroli, B., and Caroli, C. (1994) Creep, stick-slip, and dry-friction dynamics: Experiments and a heuristic model, Physical Review E. 49(6), 4973-4988.

Hess, B., Kutzner, C., van der Spoel, D., and Lindahl, E. (2008) Gromacs 4: Algorithms for highly efficient, load-balanced, and scalable molecular simulation, Journal of Chemical Theory and Computation. 4(3), 435-447.

Hilairet, N., Reynard, B., Wang, Y., Daniel, I., Merkel, S., Nishiyama, N., and Petitgirard, S. (2007) High-pressure creep of serpentine, interseismic deformation, and initiation of subduction, Science. 318(5858), 1910.

Hirose, T., and Shimamoto, T. (2005) Growth of molten zone as a mechanism of slip weakening of simulated faults in gabbro during frictional melting, Journal of Geophysical Research: Solid Earth. 110(B5)

Holdsworth, R.E. (2004) Weak faults--rotten cores, Science. 303(5655), 181.

Hoover, W.G. (1985) Canonical dynamics - equilibrium phase-space distributions, Physical Review A. 31(3), 1695-1697.

Ikari, M.J., Niemeijer, A.R., Spiers, C.J., Kopf, A.J., and Saffer, D.M. (2013) Experimental evidence linking slip instability with seafloor lithology and topography at the costa rica convergent margin, Geology. 41(8), 891-894.

Im, K., Saffer, D., Marone, C., and Avouac, J.-P. (2020) Slip-rate-dependent friction as a universal mechanism for slow slip events, Nature Geoscience. 13(10), 705-+.

Jinesh, K.B., and Frenken, J.W.M. (2006) Capillary condensation in atomic scale friction: How water acts like a glue, Physical Review Letters. 96(16), 166103.

Kawamura, H., Hatano, T., Kato, N., Biswas, S., and Chakrabarti, B.K. (2012) Statistical physics of fracture, friction, and earthquakes, Reviews of Modern Physics. 84(2), 839-884.

Kohns, M., Reiser, S., Horsch, M., and Hasse, H. (2016) Solvent activity in electrolyte solutions from molecular simulation of the osmotic pressure, Journal of Chemical Physics. 144(8)

Koop, T., Luo, B.P., Tsias, A., and Peter, T. (2000) Water activity as the determinant for homogeneous ice nucleation in aqueous solutions, Nature. 406(6796), 611-614.

Laage, D., and Hynes, J.T. (2006) A molecular jump mechanism of water reorientation, Science. 311(5762), 832-835.

Laage, D., and Hynes, J.T. (2008) On the molecular mechanism of water reorientation, Journal of Physical Chemistry B. 112(45), 14230-14242.

Landau, L.D., and Lifschitz, E.M. (1987) *Fluid mechanics*, Pergamon Press.

Lee, J.H., and Guggenheim, S. (1981) Single-crystal x-ray refinement of pyrophyllite-1tc, American Mineralogist. 66(3-4), 350-357.

Leng, Y., and Cummings, P.T. (2005) Fluidity of hydration layers nanoconfined between mica surfaces, Physical Review Letters. 94(2), 026101.

Leng, Y., and Cummings, P.T. (2006) Hydration structure of water confined between mica surfaces, The Journal of Chemical Physics. 124(7), 074711.

Liu, C., Dutta, S., Chaudhuri, P., and Martens, K. (2021) Elastoplastic approach based on microscopic insights for the steady state and transient dynamics of sheared disordered solids, Physical Review Letters. 126(13), 138005.

Liu, Y., McGuire, J.J., and Behn, M.D. (2020) Aseismic transient slip on the gofar transform fault, east pacific rise, Proceedings of the National Academy of Sciences of the United States of America. 117(19), 10188-10194.

Lockner, D.A., Morrow, C., Moore, D., and Hickman, S. (2011) Low strength of deep san andreas fault gouge from safod core, Nature. 472(7341), 82-U107.

Lopez-Lemus, J., Chapela, G.A., and Alejandre, J. (2008) Effect of flexibility on surface tension and coexisting densities of water, Journal of Chemical Physics. 128(17)

Ma, L., Gaisinskaya-Kipnis, A., Kampf, N., and Klein, J. (2015) Origins of hydration lubrication, Nature Communications. 6(1), 6060.

Marone, C. (1998) Laboratory-derived friction laws and their application to seismic faulting, Annual Review of Earth and Planetary Sciences. 26, 643-696.

Maurer, J., and Johnson, K. (2014) Fault coupling and potential for earthquakes on the creeping section of the central san andreas fault, Journal of Geophysical Research-Solid Earth. 119(5), 4414-4428.

Mazo, M.A., Manevitch, L.I., Gusarova, E.B., Berlin, A.A., Balabaev, N.K., and Rutledge, G.C. (2008) Molecular dynamics simulation of thermomechanical properties of montmorillonite crystal. Ii. Hydrated montmorillonite crystal, Journal of Physical Chemistry C. 112(44), 17056-17062.

McGuire, J.J., Collins, J.A., Gouedard, P., Roland, E., Lizarralde, D., Boettcher, M.S., Behn, M.D., and

van der Hilst, R.D. (2012) Variations in earthquake rupture properties along the gofar transform fault, east pacific rise, Nature Geoscience. 5(5), 336-341.

Mizoguchi, K., Hirose, T., Shimamoto, T., and Fukuyama, E. (2006) Moisture-related weakening and strengthening of a fault activated at seismic slip rates, Geophysical Research Letters. 33(16)

Nicolas, A., Ferrero, E.E., Martens, K., and Barrat, J.-L. (2018) Deformation and flow of amorphous solids: Insights from elastoplastic models, Reviews of Modern Physics. 90(4), 045006.

Nose, S. (1984) A molecular-dynamics method for simulations in the canonical ensemble, Molecular Physics. 52(2), 255-268.

Ortiz-Young, D., Chiu, H.-C., Kim, S., Voïtchovsky, K., and Riedo, E. (2013) The interplay between apparent viscosity and wettability in nanoconfined water, Nature Communications. 4(1), 2482.

Parrinello, M., and Rahman, A. (1981) Polymorphic transitions in single-crystals - a new molecular-dynamics method, Journal of Applied Physics. 52(12), 7182-7190.

Perfettini, H., and Avouac, J.P. (2014) The seismic cycle in the area of the 2011 m(w)9.0 tohoku-oki earthquake, Journal of Geophysical Research-Solid Earth. 119(5), 4469-4515.

Pons, A., Darnige, T., Crassous, J., Clément, E., and Amon, A. (2016) Spatial repartition of local plastic processes in different creep regimes in a granular material, Europhysics Letters. 113(2), 28001.

Putelat, T., Dawes, J.H.P., and Willis, J.R. (2011) On the microphysical foundations of rate-and-state friction, Journal of the Mechanics and Physics of Solids. 59(5), 1062-1075.

Rice, J.R., Lapusta, N., and Ranjith, K. (2001) Rate and state dependent friction and the stability of sliding between elastically deformable solids, Journal of the Mechanics and Physics of Solids. 49(9), 1865-1898.

Scholz, C.H. (1998) Earthquakes and friction laws, Nature. 391(6662), 37-42.

Shchukin, E., Pertsov, A., Amelina, E.A., and Zelenev, A. (2001) *Colloid and surface chemistry*, Elsevier, Amsterdam.

Smith, D.E., and Dang, L.X. (1994) Computer-simulations of nacl association in polarizable water, Journal of Chemical Physics. 100(5), 3757-3766.

Smith, D.E., Wang, Y., Chaturvedi, A., and Whitley, H.D. (2006) Molecular simulations of the pressure, temperature, and chemical potential dependencies of clay swelling, Journal of Physical Chemistry B. 110(40), 20046-20054.

Tambach, T.J., Hensen, E.J.M., and Smit, B. (2004) Molecular simulations of swelling clay minerals, Journal of Physical Chemistry B. 108(23), 7586-7596.

Tarling, M.S., Smith, S.A.F., Viti, C., and Scott, J.M. (2018) Dynamic earthquake rupture preserved in a creeping serpentinite shear zone, Nature Communications. 9

Thompson, P.A., Robbins, M.O., and Grest, G.S. (1995) Structure and shear response in nanometer-thick films, Israel Journal of Chemistry. 35(1), 93-106.

Tsai, J.-C., Huang, G.-H., and Tsai, C.-E. (2021) Signature of transition between granular solid and fluid: Rate-dependent stick slips in steady shearing, Physical Review Letters. 126(12), 128001.

Urbakh, M., Klafter, J., Gourdon, D., and Israelachvili, J. (2004) The nonlinear nature of friction, Nature. 430(6999), 525-528.

Vilhena, J.G., Pimentel, C., Pedraz, P., Luo, F., Serena, P.A., Pina, C.M., Gnecco, E., and Pérez, R. (2016) Atomic-scale sliding friction on graphene in water, ACS Nano. 10(4), 4288-4293.

Whitley, H.D., and Smith, D.E. (2004) Free energy, energy, and entropy of swelling in cs–, na–, and sr–montmorillonite clays, The Journal of Chemical Physics. 120(11), 5387-5395.

Xu, R.-G., and Leng, Y. (2018) Squeezing and stick–slip friction behaviors of lubricants in boundary

lubrication, Proceedings of the National Academy of Sciences. 115(26), 6560.

Xu, R.-G., Xiang, Y., Papanikolaou, S., and Leng, Y. (2020) On the shear dilation of polycrystalline lubricant films in boundary lubricated contacts, The Journal of Chemical Physics. 152(10), 104708.

Yang, Z., and Juanes, R. (2018) Two sides of a fault: Grain-scale analysis of pore pressure control on fault slip, Physical Review E. 97(2), 022906.

Zhang, L., Lu, X., Liu, X., Zhou, J., and Zhou, H. (2014) Hydration and mobility of inter layer ions of (na-x, ca-y)-montmorillonite: A molecular dynamics study, Journal of Physical Chemistry C. 118(51), 29811-29821.

Zhou, H., Chen, M., Zhu, R., Lu, X., Zhu, J., and He, H. (2020) Coupling between clay swelling/collapse and cationic partition, Geochimica Et Cosmochimica Acta. 285, 78-99.